



HAL
open science

Experimental assessment of a nonlinear, deterministic sea wave prediction method using instantaneous velocity profiles

Marion Huchet, Aurélien Babarit, Guillaume Ducrozet, Pierre Ferrant,
Jean-Christophe Gilloteaux, Eloi Droniou

► To cite this version:

Marion Huchet, Aurélien Babarit, Guillaume Ducrozet, Pierre Ferrant, Jean-Christophe Gilloteaux, et al.. Experimental assessment of a nonlinear, deterministic sea wave prediction method using instantaneous velocity profiles. *Ocean Engineering*, 2023, 281, pp.114739. 10.1016/j.oceaneng.2023.114739 . hal-04099624

HAL Id: hal-04099624

<https://hal.science/hal-04099624v1>

Submitted on 17 May 2023

HAL is a multi-disciplinary open access archive for the deposit and dissemination of scientific research documents, whether they are published or not. The documents may come from teaching and research institutions in France or abroad, or from public or private research centers.

L'archive ouverte pluridisciplinaire **HAL**, est destinée au dépôt et à la diffusion de documents scientifiques de niveau recherche, publiés ou non, émanant des établissements d'enseignement et de recherche français ou étrangers, des laboratoires publics ou privés.

Highlights

Experimental assessment of a nonlinear, deterministic sea wave prediction method using instantaneous velocity profiles

Marion Huchet, Aurélien Babarit, Guillaume Ducrozet, Pierre Ferrant, Jean-Christophe Gilloteaux, Eloi Droniou

- A nonlinear deterministic wave prediction method, based on a HOS model, is assessed.
- Surface elevation predictions are obtained from instantaneous wave-induced velocities.
- The method is validated in wave tank experiments with wave probes, ADV and ADCPs.
- Results are reliable in the prediction zone and phase information is well predicted.

Experimental assessment of a nonlinear, deterministic sea wave prediction method using instantaneous velocity profiles

Marion Huchet^{a,b,*}, Aurélien Babarit^a, Guillaume Ducrozet^a, Pierre Ferrant^a, Jean-Christophe Gilloteaux^a and Eloi Droniou^b

^aNantes Université, Centrale Nantes, CNRS, LHEEA, UMR 6598, F-44000, 1 rue de la Noë, 44 321Nantes, France

^bDynamOcean, 5 rue Louis de Broglie, 22 300 Lannion, France

ARTICLE INFO

Keywords:

Nonlinear waves
Deterministic wave prediction
Wave tank experiments
ADCP

ABSTRACT

This paper presents the experimental proof-of-concept of a nonlinear, deterministic wave prediction method. The method is based on the adapted version of the HOS-NWT wave model and uses wave-induced velocity profiles as input information on the sea state. Unlike most HOS approaches, it does not need any optimization procedure or data assimilation step to initialize the simulation. Wave tank experiments were conducted to validate the method for irregular, long-crested waves with a low significant steepness. Data was collected using wave probes, an ADV and the fifth beams of two ADCP sensors set-up with a High-Resolution mode. Despite challenging experimental conditions for the ADCPs, the method proved able to reconstruct reliable instantaneous horizontal velocity profiles from the acoustic sensor measurements. These profiles were used as boundary conditions in the wave prediction model. The sea surface elevation predicted was compared to wave probe measurements and showed good agreement all over the theoretical prediction area.

List of symbols and abbreviations

Symbol	Description	Units			
			H_s	Significant wave height	[m]
			L_x	Length of the simulation domain	[m]
			T	Duration of the sea state's reconstruction	[s]
			T_p	Peak wave period	[s]
D	Simulation domain	[-]	U	Wave-induced horizontal velocity	[m s ⁻¹]
$D_{x,t}$	Theoretical prediction zone	[-]	U_{expe}	Horizontal velocity measured experimentally	[m s ⁻¹]
ADCP	Acoustic Doppler Current Profiler	[-]	U_{num}	Synthetic wave-induced horizontal velocity provided by the numerical twin	[m s ⁻¹]
ADV	Acoustic Doppler Velocimeter	[-]	U_{rec}	Horizontal velocity reconstructed from experimental velocity measurements	[m s ⁻¹]
HOS-NWT- <i>pred</i>	Wave propagation model: version of HOS-NWT adapted for prediction	[-]	W	Wave-induced vertical velocity	[m s ⁻¹]
HOS-NWT- <i>twin</i>	Numerical wave tank based on a High-Order Spectral (HOS) method, used to create a numerical twin of the experiments	[-]	W_{expe}	Vertical velocity experimentally measured by the ADCPs	[m s ⁻¹]
C_{gmax}	Maximum group velocity considered in the wave propagation	[m s ⁻¹]	Δx	Distance between ADCPs in the wave propagation direction	[m]
C_{gmin}	Minimum group velocity considered in the wave propagation	[m s ⁻¹]	Δz	Cell size for ADCP measurements	[m]
H_n	Noise level	[m]	ϵ_c	Characteristic wave steepness	[-]
			η	Free surface elevation	[m]

*Corresponding author

 marion.huchet@dynamocean.com (M. Huchet)
ORCID(s):

η_{expe}	Free surface elevation experimentally measured by the wave probes	[m]	2016; Naaijen et al., 2018). They offer satisfying results, provided the space and time scales of propagation are short, the prediction horizon is limited and the characteristic wave steepness is small. If these conditions are not met however, nonlinear effects become significant during wave propagation and the prediction quality deteriorates (Toffoli et al., 2008; Bonnefoy et al., 2010; Zhang et al., 2017). Therefore, despite greater computation times, other approaches use partially nonlinear wave models, up to the third order (Trulsen and Stansberg, 2001; Adcock et al., 2012; Simanesev et al., 2017), or even fully nonlinear models. Among the latter, the HOS method was found to be particularly promising for nonlinear wave prediction over large space-time domains (Wu, 2004; Blondel et al., 2010), because of its high numerical efficiency and the accuracy of the results. As already pointed out by Blondel et al. (2010); Köllisch et al. (2018), with conventional HOS models, most of the computational time is spent in determining a valid initial condition for the model, from the collected wave data. This initialization step is the main obstacle to real-time prediction today, because it requires the knowledge of two independent spatial quantities: the free surface elevation and the velocity potential at the free surface. As this is hardly achievable with classical instrumentation, the velocity potential can be approximated at first order (Klein et al., 2019), introducing errors, or computed using data assimilation (Aragh and Nwogu, 2008; Blondel-Couprie and Naaijen, 2013; Yoon et al., 2016; Köllisch et al., 2018), which greatly increases the computational cost.
η_{num}	Synthetic surface elevation provided by the numerical twin	[m]	
η_{pred}	Predicted free surface elevation	[m]	
λ_p	Peak wavelength	[m]	
ϕ	Velocity potential	[s ⁻¹]	
ϕ^S	Velocity potential at the free surface	[s ⁻¹]	
σ_η	Standard deviation of the free surface elevation	[m]	
f_p	Peak frequency of the sea state	[Hz]	
f_{min}, f_{max}	Frequency bounds for the wave spectrum, used in the definition of the theoretical prediction zone	[Hz]	
h	Water depth	[m]	
x_0	Position of the velocity measurements	[m]	Another approach was recently proposed by Huchet et al. (2021) and tested numerically. The present paper builds on this previous work. It develops a nonlinear deterministic sea wave prediction method based on fixed-point velocity measurements. Rather than sea surface elevation data sets, which are most widely used (Naaijen and Wijaya, 2014; Desmars et al., 2020), the method relies on wave-induced velocity measurements to retrieve information on the incoming sea state. An instantaneous, deterministic, horizontal velocity profile is deduced from this measurements. A nonlinear wave model based on the HOS method then propagates the corresponding waves downstream. Unlike other approaches using a HOS model, here we use a formulation which was initially developed for numerical wave tank simulations, and slightly adapted to fit our purpose. As a consequence, while the initialization of the model is usually responsible for prohibitive computational effort, it is much easier here, because the simulation starts from rest and there is no need for data assimilation. In our approach, the critical step is rather to retrieve an instantaneous wave-induced velocity profile from available sensors, to feed into the wave model.
z_{max}	Z-coordinate of the highest ADCP measurements	[m]	
z_{min}	Z-coordinate of the lowest ADCP measurements	[m]	
z_{ref}	Z-coordinate of the ADV measurements	[m]	

1. Introduction

As opposed to stochastic prediction, which yields only averaged information on the wave spectrum, deterministic sea wave prediction can provide a wave-by-wave description of the sea state's characteristics: surface elevation, kinematics, wave slope, etc. This information, if available in real-time, would greatly benefit a wide range of marine applications, such as dynamic ship positioning, improving the safety of operations, or developing control strategies for wave energy converters or offshore wind turbines.

Despite recent progress in computational capabilities and the development of new oceanographic sensors, real-time deterministic wave prediction remains a challenge and several families of methods are still under investigation. Among them, methods based on Machine Learning are on the rise and show promising results (Duan et al., 2020; Zhang et al., 2022). But the currently most advanced approaches for operational purposes use propagation models based on linear wave theory, because of the very short associated computational time. Some solutions are already commercially available (Hilmer and Thornhill, 2015; Kusters et al.,

2016; Naaijen and Wijaya, 2014; Desmars et al., 2020), the method relies on wave-induced velocity measurements to retrieve information on the incoming sea state. An instantaneous, deterministic, horizontal velocity profile is deduced from this measurements. A nonlinear wave model based on the HOS method then propagates the corresponding waves downstream. Unlike other approaches using a HOS model, here we use a formulation which was initially developed for numerical wave tank simulations, and slightly adapted to fit our purpose. As a consequence, while the initialization of the model is usually responsible for prohibitive computational effort, it is much easier here, because the simulation starts from rest and there is no need for data assimilation. In our approach, the critical step is rather to retrieve an instantaneous wave-induced velocity profile from available sensors, to feed into the wave model.

As a first step, numerical studies were conducted by Huchet et al. (2021) to assess the performance of this prediction method. Promising results were obtained when using perfect, synthetic velocity data, available in the whole water column. With synthetic data only available in a portion of the water column, the results showed an increase in error but were still highly satisfactory. Provided the horizontal

velocity profiles containing information on the sea state were accurately retrieved, the whole prediction method showed high quality results, with a good reproduction of the sea surface elevation in the spatio-temporal domain theoretically accessible to prediction. The accurate restitution of the waves phase information, even for steep sea states, was an important result of these numerical tests, as it confirmed the interest of using a nonlinear wave propagation model for prediction purposes.

Following these results, the present paper reports on the experimental validation of the method on long-crested irregular waves, in a controlled wave tank environment. Velocity data were collected with an ADV (Acoustic Doppler Velocimeter) and two ADCP (Acoustic Doppler Current Profiler) sensors. This is a particularly challenging experimental set-up, because ADCPs require the presence of small particles in the water column to work properly, which are very seldom in wave tanks. However, it allows direct testing of the suitability of these instruments for the prediction method. The quality of the measurements was found to be highly dependent on the experimental conditions (namely, the homogeneous distribution of scatterers in the water column). For trials complying with this requirement, the quality of the horizontal velocity profiles reconstructed from these acoustic measurements was assessed. The prediction obtained after feeding these profiles into the wave model agreed well with the experimental measurements.

The remainder of the present paper is structured as follows: Section 2 describes the prediction method, Section 3 presents the experimental setup and the validation principle of the study conducted. Section 4 provides an analysis of the measurements collected, and Section 5 discusses the results.

2. Prediction method

The prediction method has already been studied numerically. A detailed description of the method is available in Huchet et al. (2021). Only its essential elements are reminded here for comprehension.

2.1. Assumptions and general principle

The study considers long-crested waves propagating over a constant depth h . The effects of wind forcing, wave breaking and ambient currents are not taken into account. The space domain D is defined horizontally between $x = x_0$ and $x = x_0 + L_x$, and vertically between the flat bottom $z = -h$ and the single-valued free surface position $z = \eta(x, t)$. We use a Cartesian coordinate system, (O, x, z) , set as shown in Figure 1: the horizontal axis is located at the mean water level, waves are propagating towards $x > 0$, and the vertical axis is positive-upward. Finally, we use the potential flow theory, i.e. we assume that the fluid is inviscid, incompressible and with an irrotational motion.

In this context, the method discussed here aims to provide a deterministic wave prediction, at a horizon of a few wave periods (around 20 - 40 seconds for full scale sea states). Its principle is illustrated in Figure 1. Using a fixed

measurement device deployed upstream of the area of interest, the wave-induced flow velocity is collected continuously along the water column, at a position noted x_0 . The data is used to reconstruct the profile of the horizontal component of the instantaneous fluid velocity: $U(x_0, z, t)$. This horizontal velocity profile is then passed on as a boundary condition in a deterministic, nonlinear wave propagation model. Starting from initial rest, the prediction process can then be broken down into two steps: the reconstruction of the sea state and the actual prediction.

- The reconstruction step, of duration T , is arbitrarily set in the past and is presented in Figure 1a. For $-T \leq t \leq 0$, the velocity measurements collected at x_0 in the water column are continuously updated. The boundary condition provided to the propagation model is obtained from these measurements. It is given as an instantaneous horizontal velocity profile imposed at x_0 . The model generates and propagates the corresponding waves from x_0 to the downstream area of interest.
- The prediction step is illustrated in Figure 1b. At $t > 0$, velocity data containing information on the incident waves at x_0 are no longer updated, and the boundary condition is set to zero in the wave model. Therefore, it propagates only the information collected before $t = 0$ and already present in the simulation domain.

2.2. Theoretical prediction zone

Because the information collected about the incident sea state is limited in time and space, the spatio-temporal region over which a deterministic wave prediction can be established using these measurements is also bounded. This region is called the theoretical prediction zone and is noted $D_{x,t}$ in the present article. The topic has been discussed extensively before, e.g. in Wu (2004); Naaijen et al. (2014); Qi et al. (2018); Fucile et al. (2018), so the definition provided below is directly adapted to the present case study. We simply indicate here that an accurate description of the sea state is possible only if the energy content of the wave spectrum is known. This content propagates at the wave group velocity. Therefore, besides the location and duration of wave measurements, the extent of the theoretical prediction zone also depends on the limiting group velocities of the sea state components. Assuming the wave energy is concentrated around the peak frequency of the spectrum, it becomes negligible outside some well-chosen frequency bounds f_{min} and f_{max} , and the spectrum evolution can be studied within these bounds.

In the present case study, a single, fixed measurement point upstream is located at x_0 and measures continuously for a period of time T . The corresponding theoretical prediction zone $D_{x,t}$ is defined by :

$$(x_1, t_1) \in D_{x,t} \quad \text{if} \quad -T + \frac{x_1 - x_0}{C_{g_{min}}} \leq t_1 \leq \frac{x_1 - x_0}{C_{g_{max}}} \quad (1)$$

where $C_{g_{min}} = C_g(f_{max})$ and $C_{g_{max}} = C_g(f_{min})$ are the group velocities of respectively the slowest and the fastest

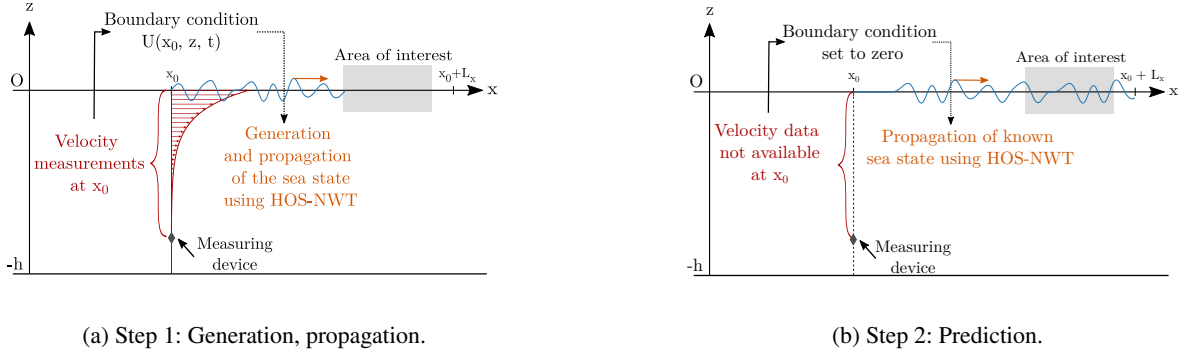
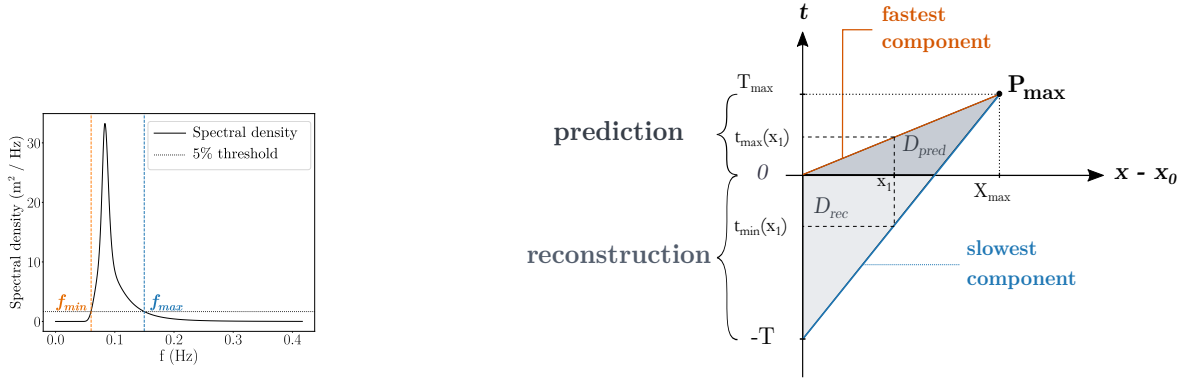


Figure 1: Proposed method for deterministic wave prediction.



(a) Example of a wave spectrum and associated f_{min} and f_{max} , bounding the retained contributions.

(b) Area theoretically accessible to deterministic wave prediction, depending on the measurement duration T and on the group speed considered.

Figure 2: Definition of the prediction zone in time and space, for a single fixed point measurement.

components of the considered sea state. At any fixed location x_1 , the prediction zone is also characterized by its temporal boundaries $t_{min}(x_1) = -T + (x_1 - x_0)/C_{g_{min}}$ and $t_{max}(x_1) = (x_1 - x_0)/C_{g_{max}}$, the latter being the maximum prediction horizon.

The total prediction zone $D_{x,t}$ can be further divided into a reconstruction sub-region D_{rec} for $t \leq 0$ and a prediction sub-region D_{pred} for $t > 0$, as illustrated in Figure 2b.

2.3. Nonlinear wave prediction model

In the present method, the information collected on the incident sea state is used to reconstruct and propagate the waves along (Ox) , using a horizontal flow imposed at x_0 . This step is performed with the open-source wave model HOS-NWT¹. This code is a nonlinear, deterministic Numerical Wave Tank based on the HOS method (Le Touz , 2003; Bonnefoy, 2005; Ducrozet, 2007; Bonnefoy et al., 2010). As shown by Ducrozet et al. (2012), the use of a Fast Fourier Transforms (FFT) solution coupled to an accelerated scheme makes the code very efficient, and the fast convergence also allows for a high accuracy in the results. HOS-NWT thus appears particularly suitable for the prediction of complex

sea states, while maintaining the possibility of reaching real-time prediction, if properly optimized. Moreover, generating waves with a numerical wavemaker is very similar to generating waves by imposing a velocity profile at a fixed location. Only minor changes were thus needed in the model to serve the targeted application. Detailed explanations of the functioning of the HOS-NWT model, as well as validation cases, are available in several works, such as Ducrozet et al. (2006, 2012). The minor modifications made to adapt it to our prediction problem are presented in Huchet et al. (2021). In the following, the general features of the code are only reminded for the sake of completeness.

In the original version of HOS-NWT, within the fluid domain D previously defined, the section $x = x_0$ corresponds to the wavemaker's rest position, and the section $x = x_0 + L_x$ represents a perfectly reflective wall. HOS-NWT runs under the potential flow assumptions introduced in section 2.1. The bottom boundary condition is a no-flow condition. The free surface boundary conditions are written in a fully-nonlinear form following Zakharov (1968). They are solved at the position of the free surface, using the order-consistent High-Order Spectral method of West et al. (1987).

¹Code available at: <https://github.com/LHEEA/HOS-NWT>

It allows a rapid and accurate resolution of the free surface equations, at an arbitrary order of nonlinearity M .

The lateral boundary conditions are expressed as Neumann (no-flow) conditions. In our adapted version of HOS-NWT, the horizontal flow $U(x_0, z, t)$, which accounts for the generation of waves, is imposed at x_0 instead of being written at the position of a moving wavemaker. As described in Section 2.1, in the prediction method $U(x_0, z, t)$ corresponds to the instantaneous horizontal velocity profile obtained from the measurements at x_0 . Finally, HOS-NWT also models the presence of an absorbing beach near the reflective wall at $x = x_0 + L_x$ (Bonnefoy et al., 2010; Ducroz et al., 2012). In a prediction context, the beach is modeled as fully absorbing and L_x is set long enough to avoid reflection in the domain.

The main advantage of using this adapted HOS-NWT model for prediction purposes is that, while having a fully nonlinear wave propagation model, there is no need for a costly optimization procedure, or data assimilation step: the procedure is simpler than determining proper initial conditions when using an HOS formulation for open domains. To initialize such simulations based on the open HOS formulation, two independent spatial quantities are required: the free surface elevation η and the surface velocity potential ϕ^S . The second quantity is usually hard to extract from field data. In contrast, in HOS-NWT the waves are continuously generated (from rest) through the boundary condition at x_0 , and the only quantity needed for this is the instantaneous horizontal velocity profile.

2.4. Horizontal velocity reconstruction

Like in many prediction methods, the main challenge is to feed the propagation model with reliable *in situ* data. Here, this means building a valid boundary condition at $x = x_0$. This condition is expressed in the form of instantaneous profiles of the horizontal velocity associated to wave propagation. A benchmark of the sensors available on the market identified ADCPs as the most suitable instruments to measure velocities in the water column. However, as ADCPs measure radial velocities (along the acoustic beam's axis), an instantaneous horizontal velocity profile is not directly available with these instruments (Huchet et al., 2021). A method was thus developed to reconstruct this quantity using the current measurement capabilities of ADCPs. It is presented here for unidirectional sea states but could be extended to multi-directional case, using more instruments, to retrieve the profile of the 2D horizontal component at a (single) given point.

Besides the four divergent acoustic beams usually present in a conventional ADCP, some recent models are also equipped with a fifth beam, oriented vertically for a bottom-mounted instrument. It can measure the instantaneous profile of the vertical component of the velocity with a good resolution, see e.g. Nortek (2022b). The method proposed here uses only the vertical beam of two ADCPs to reconstruct an instantaneous horizontal velocity profile. In the proposed measurement configuration, shown in Figure 3,

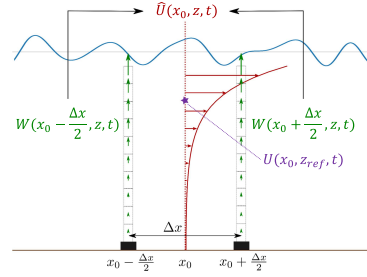


Figure 3: Reconstruction of the horizontal velocity profile $U(x_0, z, t)$ from data measured as two vertical velocity profiles $W(x_0 \pm \Delta x/2, z, t)$ and a horizontal velocity single-point measurement $U(x_0, z_{ref}, t)$.

the two ADCPs are separated by a distance Δx in the direction of wave propagation (Ox), that is small with respect to the wavelength. They measure two instantaneous velocity profiles, denoted $W(x_0 \pm \frac{\Delta x}{2}, z, t)$. The velocity measurements of both ADCPs are synchronized. Under the assumption of irrotational flow, and assuming vertical velocities are available throughout the whole water column at $x = x_0 \pm \frac{\Delta x}{2}$, an approximation $U_{rec}(x_0, z, t)$ of the instantaneous horizontal velocity profile can be written as:

$$U_{rec}(x_0, z_0, t) = \frac{\Delta z}{\Delta x} \sum_{k=1}^{N_z} \frac{\Delta W(x_0, z_{k-1}, t) + \Delta W(x_0, z_k, t)}{2} + U(x_0, z_{ref}, t) + O(\Delta x^2) + O(\Delta z^2) \quad (2)$$

where

- $\Delta W(x_0, z_0, t) = W(x_0 + \frac{\Delta x}{2}, z_0, t) - W(x_0 - \frac{\Delta x}{2}, z_0, t)$;
- z_{ref} is an arbitrary reference depth for which the horizontal velocity $U(x_0, z_{ref}, t)$ is known;
- z_k are the coordinates of the grid points on which the integration is made, dividing the interval $[z_{ref}; z_0]$ into N_z sub-intervals of length Δz . Here, Δz is constant and represents the size of the ADCPs' measurement cells.

For deep water applications, assuming the vertical velocity profiles W can be measured until the velocity becomes negligible at $z = z_{ref}$, the reference velocity $U(x_0, z_{ref}, t)$ can be set to zero without introducing much error. At intermediate depths however, a point velocimeter is useful in addition to the two profilers, to provide the horizontal reference velocity.

The proposed method uses instantaneous data, so the quality of the reconstructed velocity itself does not depend on the time discretization used. However, it assumes an accurate synchronization between the measuring devices.

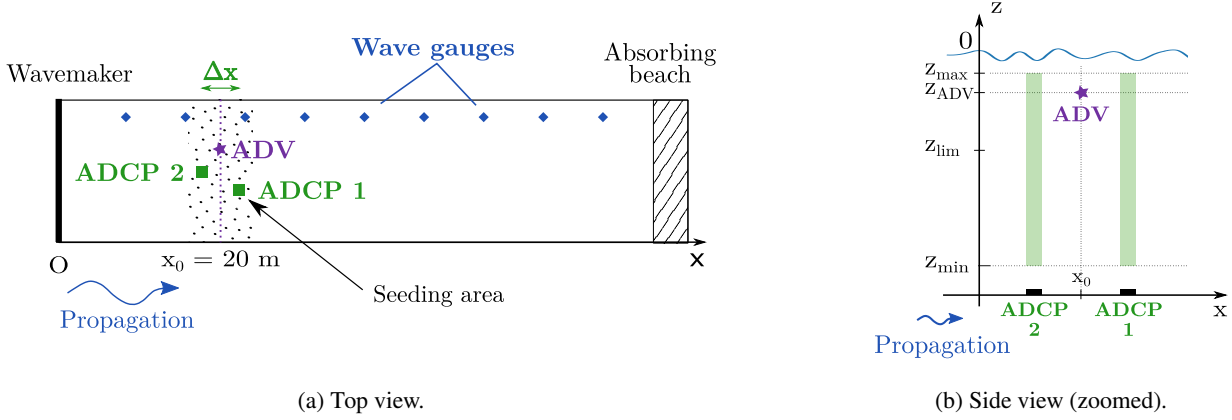


Figure 4: Schematic of the experimental set-up. Real distances are not respected. Coloured zones in Figure 4b represent the range of ADCP measurements.

3. Experiments

In this experimental validation, irregular, unidirectional waves were generated in a wave tank. The fluid velocity and surface elevation associated to these waves were measured in several locations of the tank. Two sea states characterized by a Pierson-Moskowitz spectrum were investigated. For a first validation of the method, a low characteristic wave steepness was selected: $\epsilon_c = H_s/\lambda_p = 1\%$. Two different peak periods (and thus different λ_p/h ratios) were chosen: $T_p = 2$ s (case A, hereafter) and $T_p = 3$ s (case B). This was the result of a compromise between having large enough wave velocities and enough time before measuring significant reflection from the end of the tank. The corresponding significant wave heights were $H_s = 6$ cm and $H_s = 12$ cm, respectively. For each sea state, ten phase sets were tested and lasted 350 s each.

The experiments were carried out to assess the feasibility of: i) finely measuring instantaneous vertical velocity profiles due to wave propagation, using ADCPs; ii) reconstructing instantaneous, wave-induced horizontal velocity profiles from such ADCP data; and iii) obtaining a good quality wave prediction, using these profiles as inputs in the investigated method.

To do so, surface elevation was measured using 17 resistive wave gauges. An ADV collected single-point, 3D velocity measurements at a single position (x_0, z_{ref}) in the tank, and two bottom-mounted, upward-looking ADCPs deployed on either side of x_0 (in the propagation direction) measured two distinct vertical velocity profiles. Figure 4 shows a schematic view of the general set-up.

Relatively few studies have considered the deployment of ADCPs in a tank filled with fresh water, even less for wave measurements. These studies mostly investigated averaged flow quantities, like Muste et al. (2010), or the grain size distribution of suspended sediments, as in Guerrero (2012). They highlighted that, when measuring in a fresh water tank, a major difficulty is the non-homogeneous distribution of scatterers in the water column. Depending on the application, it is sometimes possible to use adapted facilities, such

as large-scale towing tanks or tanks equipped with a recirculation and mixing system. The wave tank used in the present study does not benefit from such adaptations, and the wave measurements conducted therefore represent a very challenging setup for the use of ADCPs.

3.1. Experimental set-up

The experiments were conducted in the towing tank of Centrale Nantes, which is 140 m long, 5 m wide and 3 m deep. Waves are generated at $x = 0$ by a hinged flap rotating around an axis located at 50 cm from the bottom of the tank, and an absorbing beach limits their reflection at the other end of the tank. This beach is composed of a 5 m-long, 20% concrete slope followed by a parabolic, 3.5 m-long perforated part. Two water lines are also laid down near the beach to further reduce wave reflection. The water depth at rest is $h = 2.90$ m.

Resistance-type wave probes were installed downstream to the wave maker and recorded free surface elevation at 64 Hz, every 6 m in the propagation direction: from $x_{p1} = 24$ m to $x_{p17} = 120$ m. They were located far enough from the side wall to avoid spurious reflection and were calibrated before the trials.

Velocity measurements were collected by a single-point velocimeter (ADV), fixed at $(x_0, z_{ref}) = (20 \text{ m}, -0.54 \text{ m})$, and by two bottom-mounted acoustic profilers (ADCPs). These profilers were deployed at $x_{ADCP1} = x_0 + \Delta x/2$ and $x_{ADCP2} = x_0 - \Delta x/2$. The position $x_0 = 20$ m was set as close as possible from the wavemaker, but away from the evanescent modes, see e.g. Molin (2002).

The ADV measuring the “reference” horizontal velocity time series along Ox (with the 2 other components of the velocity) was a Nortek Vectrino. It is equipped with a four-beam head emitting convergent acoustic beams, and it is well-adapted to laboratory use. The instrument’s body was fixed to a pillar immersed in the tank, while the rod bearing the measuring head with the transmitters allowed measuring far enough from the structure for the flow not to be influenced by its presence. Measurements were collected at $(x_0, z_{ref}) = (20 \text{ m}, -0.54 \text{ m})$ with a sampling frequency of 16 Hz.

The ADCPs measured *instantaneous* vertical velocity profiles and were deployed at the bottom of the tank. Their centers were separated by $\Delta x = 5$ cm in the wave propagation direction. This is the result of a compromise between minimizing the error in Eq. (2) and the capabilities of the experimental setup, which must be able to accurately measure the vertical velocity difference $\Delta W = W(x_0 + \Delta x/2) - W(x_0 - \Delta x/2)$. In the transverse direction, the ADCPs were separated by $\Delta y = 20$ cm, their diameter being too large (15 cm) to obtain the chosen Δx spacing if keeping them aligned in the propagation direction.

The ADCPs used were Nortek Signature 1000 kHz. They were equipped with a fifth central beam, in addition to the classical 4 diverging beams. These instruments are usually deployed at sea and were not designed for laboratory trials. The measurement method remains valid, and with an adapted set-up to take this point into account, this allows to directly test the instruments' capabilities. Nevertheless, this aspect is emphasized because it is likely the cause of some difficulties that will be discussed further on.

In these trials, the 4 lateral beams were deactivated to avoid interference and only the central beam was used to measure the vertical velocity $W(x_0 \pm \Delta x/2, z, t)$. This central beam offers a High Resolution mode using a pulse-coherent method. It provides a much higher resolution and a better accuracy, at the price of a reduced achievable velocity range and / or profiling range (Rusello, 2009). This is not an issue at tank scale. Taking into account the blanking distance and the potential signal degradation near the free surface, the ADCPs provided velocity measurements between $z_{min} = -2.46$ m and $z_{max} = -0.08$ m, with a cell size $\Delta z = 2$ cm. Their sampling frequency was set to 8 Hz².

For all instruments, the start of the recording was triggered by the start of the wavemaker, ensuring the synchronization of the collected data. These were measured for 350 s after the start of the wavemaker: this is long enough to ensure that the sea state is completely established and that the waves have propagated to the area of interest, but it is still shorter than the repetition period of the wavemaker motion, which is set to 512 s. After each experiment, the wavemaker was stopped during 15 minutes to ensure a calm initial state for the following run.

Finally, ADCPs and ADVs are acoustic instruments and require backscatter from suspended particles to work properly. When using such instruments in a clear water tank, additional seeding particles are then required to ensure a sufficient return signal. Here, 10 μ m glass micro-spheres with a slightly negative buoyancy were rained down from the top of the water column around x_0 . These particles were particularly suitable for ADV measurements, but proved less efficient with ADCPs, as will be seen in Section 5.

²The maximum sampling rate is 16 Hz for the most recent instruments, but connection and hardware constraints induced some limitations in the present case.

3.2. Validation principle

The measurements made in the wave tank are used in two ways. First, the velocity data collected, $W_{expe}(x_0 \pm \Delta x/2, z, t)$ and $U_{expe}(x_0, z_{ref}, t)$, are used to reconstruct a horizontal velocity profile denoted $U_{rec}(x_0, z, t)$, following Equation (2). This experimental reconstruction is validated using a numerical twin, and is fed as input in the prediction method. Second, the wave probes' measurements $\eta_{expe}(x_p, t)$ allow to evaluate the quality of the predicted free surface elevation $\eta_{pred}(x, t)$, obtained with the investigated method.

Regarding the velocity validation, a digital twin was created for each trial to provide synthetic, reference values for the quantities of interest in the whole domain. This digital twin was generated thanks to a feature in the original version of the HOS-NWT code, which allows to specify the exact same wavemaker motion in a numerical wavetank as in the physical experiment (Bonnetoy et al., 2010; Ducroz et al., 2012). Using this HOS-NWT-*twin*, each experiment was accurately numerically modeled. The synthetic, reference horizontal velocity $U_{num}(x_0, z, t)$ was used to assess the quality of the instantaneous profile $U_{rec}(x_0, z, t)$, reconstructed from experimental velocity data.

This instantaneous horizontal velocity profile obtained from experimental data was then used to generate and propagate the waves in the prediction model described in Section 2.3, denoted HOS-NWT-*pred*. This is the version of the HOS-NWT code adapted to prediction purposes. The results obtained with the prediction model fed by experimental velocity profiles, denoted $\eta_{pred}(x, t)$, were compared to the surface elevation data $\eta_{expe}(x_p, t)$ measured by the wave gauges, to validate the whole prediction method.

The internal time step for both types of HOS-NWT simulations was around 0.02 s. The velocity profile was linearly interpolated from the reconstructed boundary condition in the prediction simulations.

Figure 5 presents a summary of the quantities measured and their use in the validation procedure.

In the prediction simulations, the velocity profiles were given as an imposed horizontal flow for the boundary condition at x_0 . The corresponding sea state was reconstructed for $T = 30 T_p$ and an additional $5 T_p$ ramp accounting for the start of the wave maker. In the common reference frame aligned on the physical tank, the wave generation was forced at $x_0 = 20$ m in the prediction model, meaning the prediction simulations were shifted in space with respect to the physical experiment and the reference simulations (which started at $x = 0$). The calculation of the theoretical prediction area was adapted accordingly and the length of the simulation domain in prediction simulations was set to $L_x = 120$ m.

4. Analysis

4.1. Reflection in the wave tank

The presence of reflection in the wave tank is evidenced by the increasing difference, over time, between the free surface measurements and the reference simulation. When restricted to periods of time before the reflected component

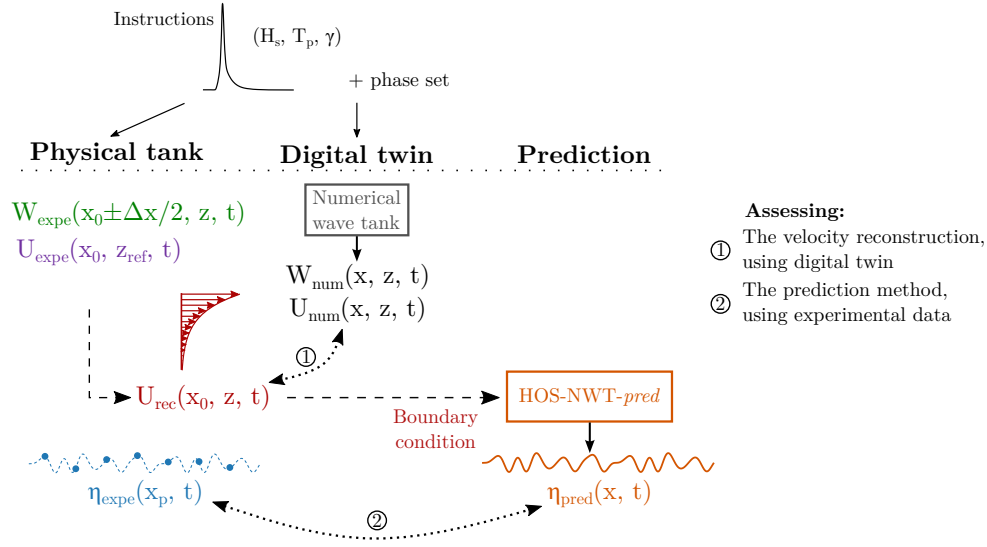


Figure 5: Overview of the experimental validation process. Each case is characterized by its frequency spectrum and associated set of phases, and the instructions are used: i) by the physical wavemaker to generate the sea state in the wave tank and ii) as input to a digital twin, numerically replicating the trial for validation purposes. The reconstructed horizontal velocity is fed as input to the prediction model.

of frequency f_{max} reaches each wave gauge, the analysis shows that the measurements agree very well with the results of the digital twin: the mean absolute difference in free surface elevation (averaged over all wave gauges) is 1.1% of H_s for case A.10, and 1.2% of H_s for case B.1. However, when considering data over a duration which includes reflection, the mean absolute difference increases respectively to 4.8% and 6.5% of H_s . Because the probe spacing is regular and very close to a multiple of $\lambda_p/2$ for both considered sea states, reflection in the experimental data could not be corrected ex-post using the method proposed by Mansard and Funke (1980).

Dedicated tests with a single regular wave train evaluated the reflection coefficient for regular waves: with a period $T = 2$ s (resp. 3 s) and an amplitude $A = 3$ cm (resp. 6 cm), a reflection of 10% (resp. 12%) in amplitude was measured.

A complementary approach, adapted from Desmars et al. (2020), measured the residual perturbations in the tank after the wave maker had stopped and the last wave components had propagated past all probes, at a time denoted t_n . Assuming that the situation is representative of the whole experiment, the recordings of the free surface elevation from N probes were used to calculate a “noise level” H_n , built on the same model as the significant wave height H_s :

$$H_n = \frac{1}{N} \sum_{i=1}^N 4\sigma_\eta(x_i, t \geq t_n) \quad (3)$$

The noise-to-signal ratio $NSR = H_n/H_s$ derived from this analysis was estimated at 10% for case A, and at 9% for case B. In Desmars et al. (2020), for the same wave steepness the measured NSR was around 20%. This may be explained by the fact that their experiment was conducted in a wider

wave tank, more likely to generate transverse disturbances because of the wavemaker flaps.

The frequency distribution of the noise was also estimated by computing the power spectral density S_n of the noisy part of the signal, obtained by averaging the results over the N wave probes. The normalized noise spectrum $S_n^* = S_n f_p / m_0$, with $m_0 = H_n/16$, is presented in Figure 6 for both sea states. The normalized target wave spectrum is also provided for illustrative purposes.

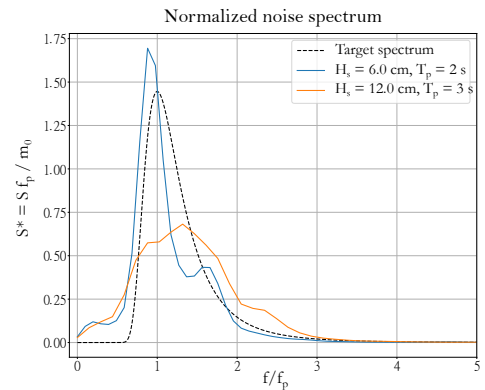


Figure 6: Normalized noise spectra.

The reflection maximum frequency is around $f_0 = 0.44$ Hz in both sea states, i.e. $0.9f_p$ for case A and $1.3f_p$ for case B. The reflected energy is more concentrated around the peak for case A than for case B. In both cases, noise at low frequencies is present but at a much lower level than around the peak. It can be mitigated by processing the data with a high-pass filter, provided the cut-off frequency does

not mask information related to energetic components of the wave spectrum.

As the effects of reflection are particularly important around f_0 , whenever possible the analysis was restrained to the instants preceding the arrival of the reflected wave of frequency f_0 at the point of interest. This is the case when evaluating the quality of the reconstructed horizontal velocity profile: the position of the instruments around x_0 , i.e. close to the wavemaker, allows a quick establishment of a complete sea state and the measurements duration is thus sufficient to analyze the results. Unfortunately, this is not possible for the prediction results. This is because the time needed to establish a complete sea state at the most downstream probes (which are used to evaluate the prediction on η) is greater than the travel time of the reflected wave of frequency f_0 (which is the time taken by the frequency component f_0 to reach the downstream probes after reflection on the beach).

4.2. Data quality control

4.2.1. Overview

The wave gauges were calibrated before the trials and their use in this experimental setup is classical: therefore, applying a perfect low-pass filter at $f_{cut} = 8$ Hz is sufficient after data collection.

For ADV as well as ADCP measurements, in addition to raw velocity data the instruments also provide auxiliary quantities that help evaluate the data quality. One of them is the correlation, which is “a statistical measure of how similar the received signal is to itself at a delayed time” (Nortek, 2022b). The exact definition of correlation varies depending on the instruments and on manufacturers, but the principle remains the same. The higher the correlation, the most reliable the data, because it means the instrument is more likely to have measured correctly the pulses it emitted, and determined a valid velocity. Drops in correlation allow to identify events when the signal can be too weak or too blurred to allow collecting good data.

Here, the seeding system designed to provide a high concentration of scatterers in the wave tank worked very well for the ADV measurements, as expected since this instrument is routinely used in laboratory experiments. The correlation values associated to the ADV measurements remain higher than 80% for all beams from all trials, when the advised minimum threshold is 70% in usual applications (Nortek, 2022a). It is even higher than 95% for more than 97% of measurements from beam 1³, indicating excellent data quality. For this ADV data, a (perfect) low-pass filter at $f_{cut} = 8$ Hz is also sufficient.

In contrast, the quality of the vertical velocity profiles measured by the ADCPs in the wave tank environment is overall disappointing. Figure 7 shows an example of raw ADCP data: the first subplot presents the vertical velocities measured by the instrument and the bottom subplot shows the values of associated correlation. Generally, correlation

is used in quality control to identify the reliable data range. It also helps spotting outliers, discarding any velocity data point whose associated correlation falls below a user-defined threshold. As can be seen in Figure 7, the data quality is unequal, very poor in some areas, and calls for a closer look.

4.2.2. Processing of ADCP data

Numerous outliers are visible in the data, and the signal quality is not homogeneous. It varies with both the trial and the depth, with a particularly poor data quality at the bottom of the water column (very low correlation). This means this is not a problem of measurement range. Besides, despite legitimate concerns due to the proximity between the ADCPs, there were no recognizable signs of interference between the beams. These would translate into distinct and consistent areas of poor correlation; what is observed here looks more like patterns induced by flocks of slowly moving scatterers, as shown by the stratified patterns.

Regardless of the application, ADCP data need to undergo a proper quality control procedure before they can be analyzed. This is especially true here, as we need the data to be accurate enough to reconstruct an instantaneous horizontal velocity profile, which should describe the deterministic influence of waves in the water column. Here, the signal is too noisy for a classical spectral filtering to be useful.

The quality check conducted started by removing all data points associated with a correlation lower than 80%. Then, because phase-resolved wave prediction is possible only if a sufficient amount of information is available from both ADCPs at the same time, only trials where both ADCPs passed the correlation test more than 90% of the time were kept. This left only one suitable case for $T_p = 2$ s: A.10, and two for $T_p = 3$ s: B.1 and B.3. For the sake of conciseness, only cases A.10 and B.1 are presented in the following.

Another outlier detection round was conducted cell by cell, using first the criterion $|W_{outlier}(z, t) - \langle W(z) \rangle| > 6 \sigma_W(z)$, then the Phase-Space Thresholding Method (PSTM). It is an iterative detection method that was first proposed by Goring and Nikora (2002) for the despiking of ADV data time series. It uses 3D Poincaré maps and the first two time derivatives of the signal. The incorrect data points spotted were replaced by interpolation. Finally, the resulting W arrays were smoothed by vertically fitting a *sinh*-type function on each instantaneous profile. More detail on the whole procedure can be found in Appendix A. What can be noted here, however, is that the processing steps conducted in the procedure described are not yet compatible with real-time, as for example the PSTM is applied *a posteriori*.

This specific treatment is more intensive than what is usually done for ADCP data, but is necessary here due to the challenge of collecting good quality data in a lab environment with fresh clear water. Data quality control in real conditions is expected to be more simple, and should be possible with conventional techniques for raw ADCP data (see e.g. Furgerot et al. (2020)), which rely on ancillary quantities such as correlation. This type of data is provided from the instrument’s internal processing, as a direct output

³According to the Vectrino’s orientation, this beam directly provides the horizontal velocity.

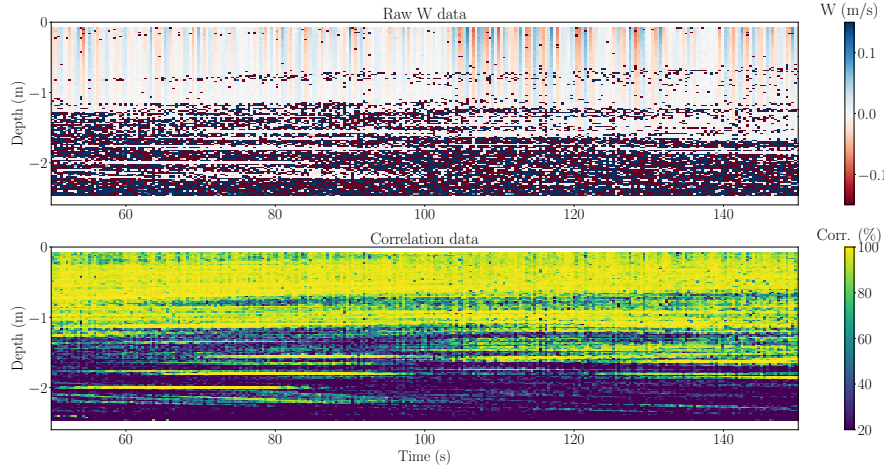


Figure 7: Overview of raw ADCP data and associated correlation for one trial.

of the ADCP measurements. It is thus available at the same time as the velocity data itself and requires no additional processing time.

4.3. Horizontal velocity reconstruction

After data processing, the instantaneous horizontal velocity profile $U_{rec}(x_0, z, t)$ is computed from the single-point horizontal velocity measurements $U_{expe}(x_0, z_{ref}, t)$ provided by the ADV, and the two vertical velocity profiles $W_{expe}(x_0 \pm \Delta x/2, z, t)$ measured by the ADCPs. Here, preliminary tests have shown that using W data below z_{ref} did not improve the quality of the reconstruction. This is mostly due to the inconsistent quality of ADCP measurements, especially further from the surface. Besides, the integration error on z accumulates when moving away from z_{ref} . The horizontal velocity profile is then reconstructed using Equation (2) only between z_{ref} and z_{max} . Discarding data below z_{ref} means that only $|z_{ref}|/h \approx 18\%$ of the profile is sampled experimentally⁴. However, this is where the most important information on waves is found. In the rest of the profile, a vertical fitting is run for each time step, where the fitting function is a 3-component approximation of the expression of the horizontal velocity in the linear wave theory. Finally, a perfect high-pass filter with a cut-off frequency $f_c = 0.1$ Hz is applied to the reconstructed horizontal velocity, removing any low frequencies present in the signal that would not be useful for describing the sea state. Note that applying a perfect (Fourier) filter is not compatible with real-time data processing, as it is non-causal. This would need to be improved in the future.

4.4. Error indicators definitions

As stated in Section 4.2, the quality of velocity data is variable because the scatterers concentration was not homogeneous in the measurement area, despite the seeding system being designed to minimize this problem. This led

⁴This represents $|z_{ref}|/\lambda_p \approx 9\%$ (resp. $\approx 4\%$) of a peak wavelength for cases A (resp. for cases B), which means velocity orbitals have not yet faded away.

to noisy measurements, and thus to a high proportion of missing data in some areas. Analysis of the experimental data showed that this heterogeneity is visible within a single trial: the upper part of the water column is better covered than the bottom. But experimental conditions also changed from one tank test to another. Consequently, differences in data quality are found between trials. In the following, the analysis of the results is then restricted to the trials for which the experimental conditions allowed the best quality data to be collected: one for each sea state tested. This reduces the number of factors influencing the results and makes the analysis more simple.

4.4.1. On velocity reconstruction

The reconstructed horizontal velocity profile, $U_{rec}(x_0, z, t)$, is compared with the data provided by the reference simulations, $U_{num}(x_0, z, t)$. Parasitic reflections at the end of the physical wave tank are difficult to reproduce accurately in these simulations (see Section 4.1). To minimize their influence, the results of the velocity reconstruction are thus analyzed only for the period T limited by:

- the time when a complete sea state is established at x_0 : $t_{min} = x_0/C_g(f_{max})$;
- the time when the waves of frequency f_p arrive at x_0 after being reflected by the beach at $x = x_0 + L_x$, which are likely to be the main contributor to the parasite waves: $t_{max} = (2L_x - x_0)/C_g(f_p)$.

With f_{max} selected to neglect the components responsible for less than 5% of the maximal spectrum density, this corresponds to a total reconstruction period $T = 126$ s $\approx 63 T_p$ for cases A ($T_p = 2$ s), and $T = 70$ s $\approx 23 T_p$ minimum for cases B ($T_p = 3$ s). The error indicator selected provides a normalized error profile averaged over this time range, during which reflection should be minimal:

$$\epsilon_{NRMS}(z) = \left[\frac{\int_0^T [U_{rec}(x_0, z, t) - U_{num}(x_0, z, t)]^2 dt}{\int_0^T U_{num}(x_0, 0, t)^2 dt} \right]^{1/2}$$

(4) defined by:

$$C(\tau) = \frac{1}{t_{max} - t_{min}} \int_{t_{min}}^{t_{max}} \eta_{pred}^*(x_p, t) \eta_{expe}^*(x_p, t + \tau) dt \quad (7)$$

where U_{rec} is the reconstructed velocity, U_{num} is the velocity provided by the digital twin, and T is the time range considered for the reconstruction in each trial.

4.4.2. On wave prediction

This section introduces several quality metrics for the deterministic prediction of free surface elevation. Some of them are classical error indicators, others were provided to allow the comparison of our results to previous studies.

Following Desmars et al. (2020), the accuracy of the predicted wave field is assessed with the misfit indicator $\mathcal{E}(x, t)$:

$$\mathcal{E}(x, t) = \frac{1}{N_s} \sum_{i=1}^{N_s} \frac{|\eta_{pred,i}(x, t) - \eta_{expe,i}(x, t)|}{H_s} \quad (5)$$

where η_{pred} is the predicted surface elevation, η_{expe} is the surface elevation measured by the wave probes and N_s is the number of samples used to get an average misfit. Ideally the N_s samples should be completely independent, i.e. recorded from different wave fields with random phases sets. Because of experimental costs and of the varying experimental conditions, this was not possible in this study. Instead, here the different phase sets are replaced by N_s samples from a single trial, taken as partially overlapping sub-segments of the time series. Each sub-segment is shifted from the previous one by a duration $\Delta t < T$. It has been shown (e.g. in Naaijen et al. (2014) and Desmars et al. (2020)) that this method allows statistical averaging, provided the total measurement period is long enough and reflection does not affect the results too much.

The information used to evaluate the misfit $\mathcal{E}(x, t)$ then covers a total duration of $T_{tot} = T + (N_s - 1)\Delta t$. A convergence study (not shown here) determined that in our case, with $\Delta t = 1$ s the prediction error $\mathcal{E}(x, t)$ is fully converged for $T_{tot} \approx 60T_p$, but is already stable from $T_{tot} \geq 50T_p$, which is then the criterion defined here. This is important because in this set-up, the longer we record the signal, the more important reflection problems become.

From the error field $\mathcal{E}(x, t)$, a prediction error at any given location x is obtained by averaging $\mathcal{E}(x, t)$ over the prediction zone:

$$\mathcal{E}^P(x) = \frac{1}{t_{max}(x) - t_{min}(x)} \int_{t_{min}}^{t_{max}} \mathcal{E}(x, t) dt \quad (6)$$

where $t_{min}(x)$ and $t_{max}(x)$ are respectively the beginning and the end of the theoretical prediction zone at the considered location.

Still following Desmars et al. (2020), a complementary metrics is also provided in the form of a cross-correlation indicator. Cross-correlation is well adapted to deterministic comparison because it measures the similarity between two time series: here, the free surface elevation recorded by a given probe and the corresponding prediction at this location. At any point x_p , the time-averaged cross-correlation is

defined by:

where $\eta_{pred}^* = \eta_{pred} / \sigma_{\eta_{pred}}$ is the free surface elevation predicted by the investigated method, normalized by its standard deviation over the (temporal) prediction zone, and $\eta_{expe}^* = \eta_{expe} / \sigma_{\eta_{expe}}$ similarly refers to the normalized free surface elevation measured by the wave probes. The calculation gives the correlation factor C as a function of a time delay τ . Its maximum C_{max} , and the time lag T_s for which it is reached, allow to estimate respectively the similarity in shape and amplitude between the signals, and the phase shift of one with respect to the other. The cross-correlation of a signal with itself will thus give a maximum amplitude $C_{max} = 1$ for a zero time lag. Here, for each case considered, C_{max} and T_s are calculated for all the N_s predictions obtained from the data sub-samples, and averaged over these N_s simulations for each probe location.

Finally, to allow further comparisons with previous studies, another classical indicator is provided, relying on correlation as well. As in (5), it is a field indicator, expressed as:

$$c(x, t) = \frac{1}{N_s} \sum_{i=1}^{N_s} \eta_{pred,i}^*(x, t) \eta_{expe,i}^*(x, t) \quad (8)$$

where, unlike in (7), σ_{η} the standard deviation of η is computed over the whole measurement time and not only within the $[t_{min}; t_{max}]$ time range.

5. Results

This section presents the findings of the experimental validation: first for the reconstruction of the horizontal velocity profile, then for the prediction of free surface elevation. As a reminder, because of diverging data quality between trials, the analysis of the results is restricted to one trial per sea state.

5.1. Horizontal velocity profile

After the data quality control procedure, trials A.10 and B.1 still show a high proportion of valid ADCP data near the free surface for both instruments. They are therefore interesting examples, especially as they were carried out one right after the other and the experimental conditions are likely to be very similar between these two trials.

Figure 8 presents the error profiles obtained for these cases, respectively for case A.10 ($T_p = 2$ s, (a)) and case B.1 ($T_p = 3$ s, (b)). This error is obtained by comparing indirect experimental results (i.e. the velocity reconstructed from experimental data) with the reference U_{num} from HOS-NWT-twin. The coloured area indicates the depth range over which the ADCP data were used. For each case, three profiles are shown:

- The dashed orange profile (---) is obtained by using only measurements in the reconstruction: vertical

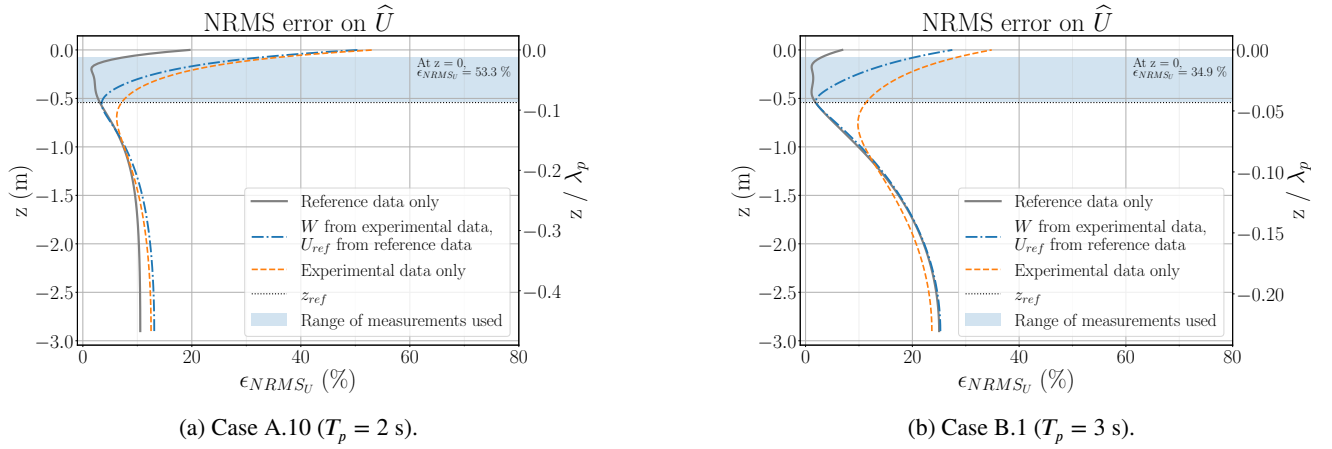


Figure 8: Error profiles for U_{rec} , computed from one single realization for each sea state. (—) W and U_{ref} from synthetic, reference data. (---) W from experimental data, U_{ref} from synthetic data. (- - -) W and U_{ref} from experimental data.

velocities $W_{expe}(x_0 \pm \Delta x/2, z, t)$ provided by the two ADCPs for $z \in [z_{ref}; z_{max}]$; reference horizontal velocity $U_{expe}(x_0, z_{ref}, t)$ given by the ADV.

- The solid gray profile (—) is obtained by using only synthetic data from the digital twin, with the same “measurement” configuration as for the experimental setup (*i.e.* W_{num} data restricted to $z \in [z_{ref}; z_{max}]$). It represents the minimum error theoretically achievable with the reconstruction method for a given measurement configuration, assuming perfect data. It also highlights the consequences of data not being available outside $[z_{ref}; z_{max}]$, without the influence of measurement errors.
- The dashed blue profile (---) is obtained by replacing the data from the ADV by the data provided by the digital twin: $U_{num}(x_0, z_{ref}, t)$. This eliminates the measurement error of the ADV from the evaluation of the reconstructed profile, and allows to focus solely on the performance of the ADCPs.

The results obtained with purely experimental data show that for both cases, the error is minimal around $z = z_{ref}$ and increases both upwards and downwards from there. Towards the surface, the increase is sharp, while it is smoother towards the bottom.

Around $z = z_{ref}$, the horizontal velocity is directly provided by the ADV. The fully experimental error (in orange) does not reach zero however, because it compares ADV measurements with the horizontal velocity provided by the digital twin: the discrepancy between measurements and synthetic data leads to an error of 6.2% at z_{ref} for case A.10, and 11% for case B.1. Because the NRMS error is quadratic, a comparison of time series at this depth (not shown here) would show that these error levels actually reflect a very good agreement between the two quantities.

The synthetic (gray) and semi-experimental (blue) error profiles never reach zero either, even at z_{ref} . This is due to the vertical fitting step (see Section 4.2.2), which makes the

velocity at z_{ref} slightly different from $U_{num}(x_0, z_{ref}, t)$ in these profiles. It is also responsible for slightly shifting all error minima away from z_{ref} .

In the lower part of the water column, the experimental and the synthetic error profiles are similar: in this area, the error is mainly driven by the need for extrapolation caused by missing data. As already shown in Huchet et al. (2021), the quality of the reconstruction at these depths is however not the main problem: around $|z|/\lambda_p \approx 0.3$, the velocity amplitudes involved are lower and contain less useful information for the generation of the sea state than in the upper part of the water column.

Between z_{ref} and z_{max} , both the fully experimental (orange) and the semi-experimental (blue) error profiles show a sharp increase: up to 53% for case A.10 and to 35% for case B.1, at $z = 0$, for the experimental error. This confirms that the precision of ADCP measurements is a determining factor in the quality of the reconstructed velocity, as expected. By contrast, the purely synthetic error (in gray) barely varies in this range where ADCP velocity measurements are available. The sudden increase of the synthetic error close to the free surface is due to the lack of data in the last cm below $z = 0$ ⁵.

Finally, close to the free surface, the experimental error is higher for $T_p = 2$ s than for $T_p = 3$ s. The velocities involved are lower for $T_p = 2$ s, so measurement errors on $W_{ADCP_{1,2}}$ are proportionally greater, especially for small orbital amplitudes. Besides, with no measurements available right below the free surface, we are blind to small wavelengths, which results in a poor resolution of very short waves. This has a greater impact on sea states with small peak periods, because such waves are proportionally more important to accurately describe these sea states. This phenomenon is also visible in the synthetic error profiles.

The error difference is illustrated in Figure 9, which presents time series of reconstructed horizontal velocities at

⁵As verified in dedicated tests, this increase is already visible just below $z = z_{max}$ because the vertical fitting step mentioned in Section A.3 induced small modifications of the profile in the shaded area.

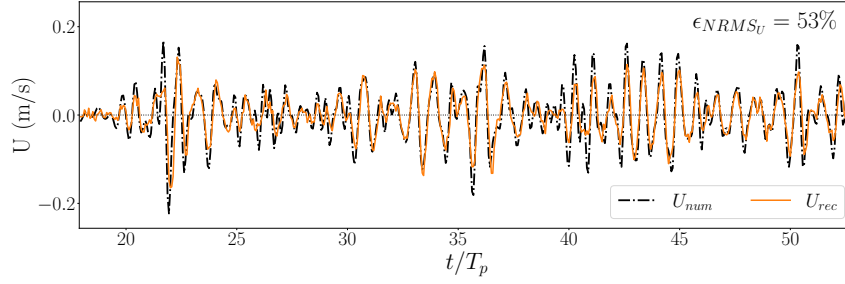
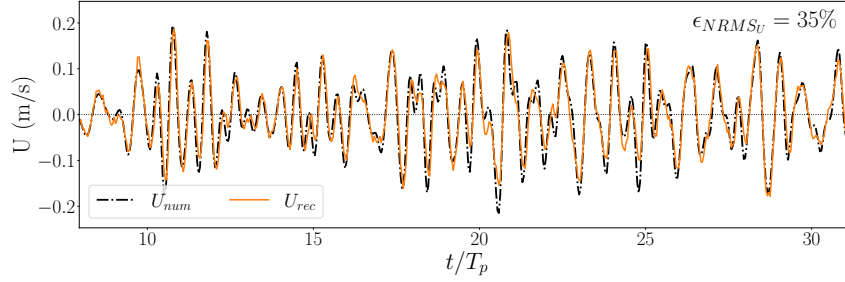

 (a) Case A.10 ($T_p = 2$ s).

 (b) Case B.1 ($T_p = 3$ s).

Figure 9: Time series of reference (U_{num}) and reconstructed (U_{rec}) horizontal velocities at $z = 0$.

$z = 0$, for $T_p = 2$ s and for $T_p = 3$ s. The difficulties in resolving short waves are clearly visible (e.g. around $t/T_p \approx 37 T_p$ for case A.10), and are more important in case A.10 than in case B.1. Even with an error around 55% however, the main patterns of the velocity signal are correctly reproduced for the larger waves. This suggest the relatively high error value accounts for the poor resolution of small waves.

In a real-scale deployment, ADCP measurement errors of this magnitude are anyway unlikely. Indeed, using an ADCP in a reduced-scale, freshwater tank represents a rather difficult case study, compared to normal operating conditions. However, in our wave tank context it remains to be seen what quality of prediction can be reached with the velocity profiles reconstructed under such experimental conditions. This topic is explored in the next subsection.

5.2. Wave prediction

To give a first overview of the results, time series of surface elevation predictions are compared to wave probe measurements for both sea states studied, in Figure 10 (case A.10) and Figure 11 (case B.1). In each case, the data subsegment used as an illustration was selected to be consistent with the mean characteristics of the obtained prediction. These mean characteristics are presented in the following figures: Figure 12 shows the misfit indicator $\mathcal{E}(x, t)$, Figure 13 shows the correlation map $c(x, t)$ as an alternative metrics, Figure 14 shows the mean prediction error at each probe $\mathcal{E}^P(x_p)$, and Figure 15 shows the overall correlation magnitude C_{max} and associated time shift T_s .

Overall, the predicted free surface elevation agrees well with the wave probes' measurements in the prediction zone.

Discrepancies are visible for small amplitude waves. Figure 10 and 11a show examples of very good agreement between the predicted and the measured waves, although case A.10 shows a tendency to underestimate wave amplitudes by around 4% of H_s . This behaviour is consistent with the underestimation of the reconstructed velocity amplitudes already visible in Figure 9a. This bias was not detected for case B.1. The missing velocity data between z_{max} and $z = 0$ are likely the cause of this phenomenon, as it means short waves are not properly accounted for, especially with $T_p = 2$ s.

In the representative example time series displayed in Figure 10 and Figure 11, the quality of the prediction decreases outside the prediction zone, as information on frequency components lower than $f_{min} = 0.67 f_p$ are not available any more. This is consistent with the spatio-temporal evolution of the average misfit presented in Figure 12, which confirms that the prediction zone is a relevant indicator of where a reliable prediction can be generated. The figure suggests that the frequency boundaries selected for this case study might even be too conservative, especially for case A.10. Even outside the prediction zone, the observed deterioration is progressive: except when small and very irregular waves are present like in Figure 11b, the method correctly reproduces the arrival instants of the main waves, even some time after the maximum theoretical prediction horizon.

Looking at averaged parameters, Figure 14 shows that the mean prediction error $\mathcal{E}^P(x)$ provided by the new prediction algorithm lies between 5 and 9.5% of H_s , depending on the sea state and the position of the probes considered.

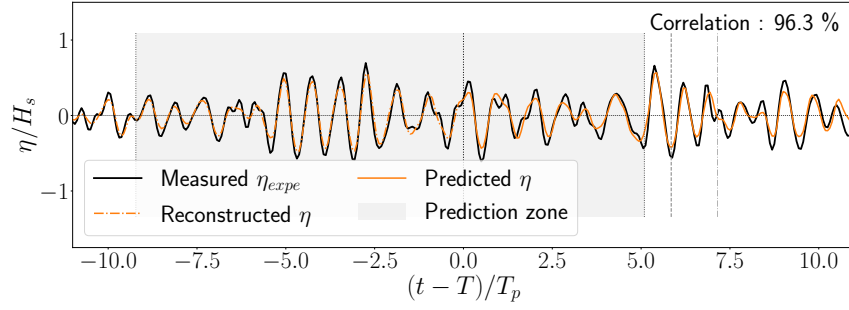
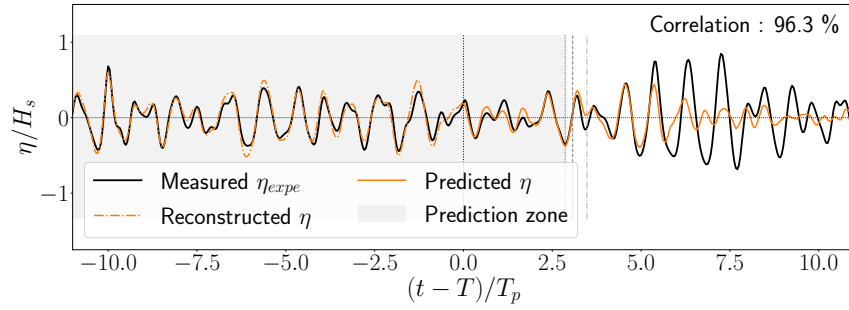
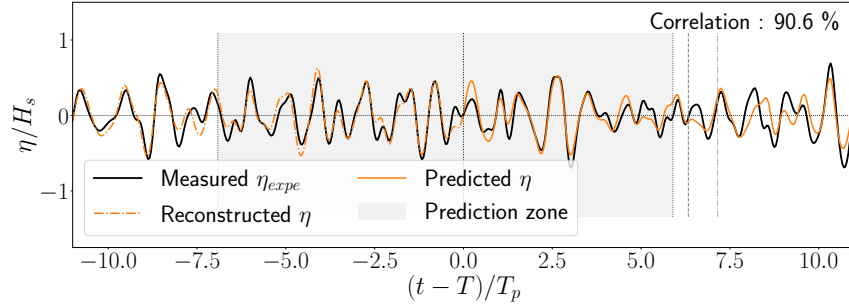


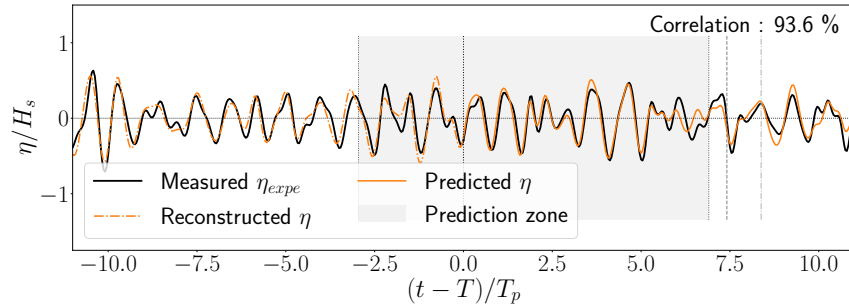
Figure 10: Case A.10. Comparison of representative $\eta_{expe}(t)$ and $\eta_{pred}(t)$ time series at $x_p = 48$ m, i.e. $4.5 \lambda_p$ downstream of x_0 . At selected location, the equivalent of $\mathcal{E}^P(x)$ averaged on one sample only is 7.2%. Corresponding $C_{max} = 96\%$ and $T_s/T_p = 0$. Vertical grey lines (---) and (---) outside the prediction zone indicate prediction horizons for alternative frequency bounds selected at respectively 25% and 75% of the energy peak, instead of 5%.



(a) At $x_p = 54$ m i.e. $2.7 \lambda_p$ downstream of x_0 . Equivalent $\mathcal{E}^P = 5.4\%$, $C_{max} = 96\%$, $T_s/T_p = -0.01$.



(b) At $x = 90$ m i.e. $5.6 \lambda_p$ downstream of x_0 . Equivalent $\mathcal{E}^P = 8.5\%$, $C_{max} = 91\%$, $T_s/T_p = -0.01$.



(c) At $x = 102$ m i.e. $6.5 \lambda_p$ downstream of x_0 . Equivalent $\mathcal{E}^P(x) = 9.3\%$, $C_{max} = 94\%$, $T_s/T_p = -0.03$.

Figure 11: Case B.1. Comparison of representative $\eta_{expe}(t)$ and $\eta_{pred}(t)$ time series at three locations in the prediction area. Vertical grey lines (---) and (---) outside the prediction zone indicate prediction horizons for alternative frequency bounds selected at respectively 25% and 75% of the energy peak, instead of 5%.

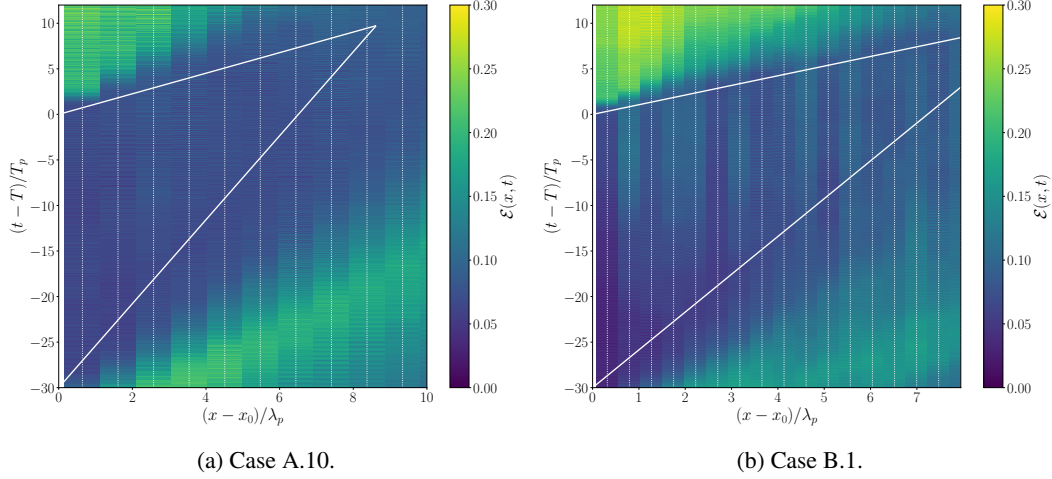


Figure 12: Map of $\mathcal{E}(x, t)$ for the two trials considered. Dashed vertical lines show the position of the probes. Solid lines indicate the prediction zone for a reconstruction period of $30 T_p$. Frequencies f_{min} and f_{max} are associated to the extreme group velocities bounding the prediction zone: they are chosen so that outside these frequency bounds, each component's spectral density is less than 5% of the wave spectrum's peak density.

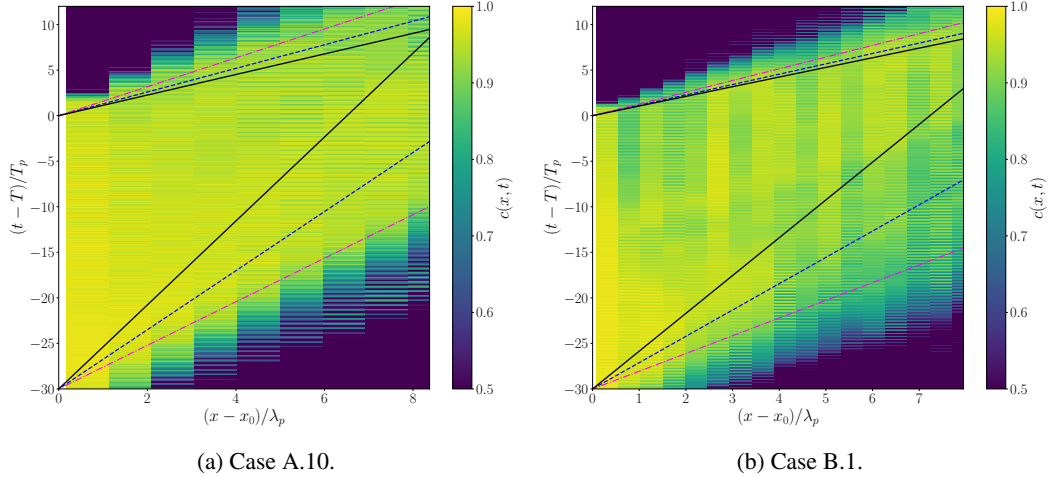


Figure 13: Map of $c(x, t)$ for the two trials considered. Black solid lines indicate the prediction zone for a reconstruction period of $30 T_p$. Outside the limit frequency bounds, each component's spectral density is less than 5% of the wave spectrum's peak density. Dashed lines (---) and (---) show alternative prediction zones for frequency bounds selected using density thresholds of respectively 25% and 75% of the peak density.

Case A.10 shows a slight but rather constant increase in the prediction error with propagation distance, from 6 to 8.5 %. Variations of \mathcal{E}^P along x are larger for case B.1, maybe because T_{tot} represents a smaller number of T_p for this case. Extending the total recording period could smooth the results but would increase the influence of parasitic reflection.

As a complementary information on the prediction's quality, the correlation indicators separate the error in amplitude and the error in phase. Results are presented in Figure 15.

The match is overall very good between the prediction and the measurements for each probe located in the theoretical prediction area, with a correlation factor C_{max} greater than 0.9 in most cases. For case A.10 and $(x - x_0)/\lambda_p \approx 8.4$,

the very high and dubious value of C_{max} is probably due to the small theoretical prediction duration at this location (see prediction zone in Figure 12a), limiting the relevance of the statistical metrics.

The phase shift remains very close to zero for both sea states and at all studied locations. The low steepness of the sea states tested ($\epsilon_c = 1\%$) was not likely to induce large errors in the wave speeds, even if we were using a linear wave model, so this result was expected. But it is worth checking, as a correct phase information is an essential aspect of a good deterministic wave prediction, especially when aiming to develop control systems.

Figure 10 and 11a are representative examples of a high correlation and a small time shift. A weaker correlation associated with a near-zero time shift, as in Figure 11b, is

often due to the presence of short waves in the prediction area (around $t/T_p = 5$), or to small waves superimposed on larger ones (around $t/T_p = -2$), which are not reproduced correctly by the prediction simulations. The main waves, on the other hand, remain fairly well resolved. A high correlation associated with a non-zero phase shift translates into a small offset in the arrival time of the wave crest, visible for some large waves around $t/T_p = 1$ and 4 in Figure 11c.

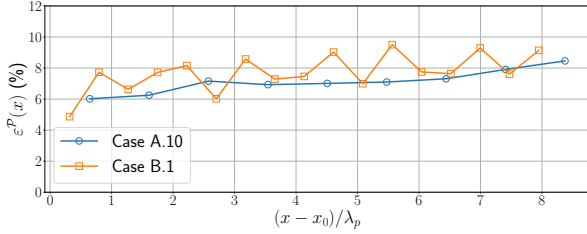


Figure 14: Prediction error for cases A.10 and B.1. Here, $T_{tot} = 57 T_p$ for A.10, $T_{tot} = 50 T_p$ for B.1 and $\Delta t = 1$ s.

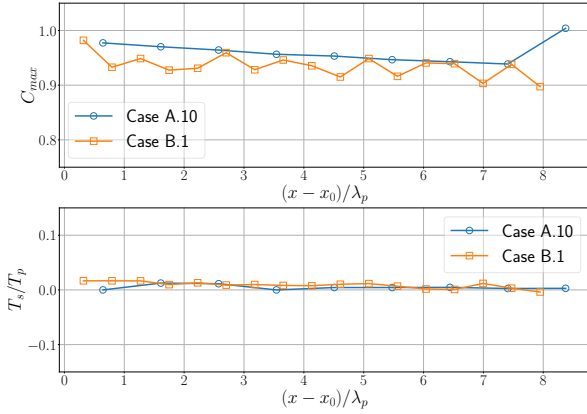


Figure 15: Correlation between the measured and predicted free surface elevation time series for cases A.10 and B.1. Top: correlation magnitude. Bottom: phase shift, as a fraction of T_p . Values are averaged over the simulations using data subsamples.

6. Discussion

As shown in Figure 13, Figure 10 and Figure 11, the 5% threshold initially selected to define the frequency bounds, and thus the prediction zone, seems too conservative. These figures show possible extensions of the cut-off frequencies with thresholds up to 75% of the energy peak. The spectra used in the experiments were Pierson-Moskowitz spectra, which are rather sharp and whose energy is concentrated around the peak, especially at low frequencies. Therefore the value of f_{min} can only be increased carefully, at the risk of missing high-energy components. However, even with the highest threshold tested (which led to $f_{min} = 86\% f_p$), the prediction quality remains reasonable. The spectrum is not as sharp for $f > f_p$, so the effects of extending the cut-off

frequencies are more visible in the lowest part of the prediction zone i.e., at the start of the (reconstruction) – prediction. The largest alternative prediction zone, shown in Figure 13, still allows a rather good agreement with the correlation pattern. This only means that a shorter measurement time is needed to obtain a meaningful reconstruction of the sea state, which is of less interest in the context of wave prediction.

Comparing the experimental results presented in Section 5.2 with the literature is not straightforward, as prediction approaches can be very different from one another. As an example, in the work of Desmars et al. (2020), information on the incident waves is collected over a spatio-temporal area rather than at a single point, and prediction errors are calculated at locations relatively close to the measurement area.

In Figure 14, our results show errors in the same order of magnitude as in their Figure 15, but with slightly greater values: in their work, $\epsilon^P(x)$ varies from 3.5 to 6.4% depending on the measurement probe and the sea state considered.

The most obvious cause for greater errors in our case is the imperfect quality of the boundary condition fed into the nonlinear propagation model, due to noisy and incomplete velocity measurements in the water column. The post-processing step was not able to completely abolish this difficulty: the consequences were already visible in Section 5.1, with a boundary condition of poorer quality than when reconstructed from synthetic data.

A second reason is the presence of reflection in the physical wave tank. Indeed, the prediction method considered here uses a velocity measurement device upstream of the prediction area. It can thus only consider the propagation of waves towards increasing x . In the tank, despite the absorbing beach, reflected waves are propagating towards decreasing x (the reflection coefficient has been estimated at approximately 10 - 12% of amplitude for regular waves, see Section 4.1). These reflected waves cross the prediction area before being measured by the sensors around x_0 , which prevents from taking them into account. As the prediction simulations are compared to the measurements from $t \geq T_{ramp} + x_0/C_{gmin}$, reflection due to the f_p frequency component, which is the main contribution, is present from the start.

As a side note, the retrieved horizontal velocity profile was evaluated on a restricted time span in Section 2.4, to limit the influence of reflection. This way, only the measurement capabilities of the sensors and the relevance of the reconstruction method were assessed. With reflection being more and more present over time in the physical wave tank, the reconstruction error calculated in Section 2.4 is not a true indicator of the overall fidelity of the boundary condition really passed to the wave prediction model.

The results presented in this work showed that, provided adequate experimental conditions are met, the proposed prediction method can produce good quality predictions of the sea surface elevation, up to a few peak periods ahead, for moderate sea states characterized by different λ_p/h ratios. In Section 5.1, the error on the reconstructed horizontal

velocity profile was greater in the upper water column for case A ($T_p = 2$ s). But the averaged error indicators showed a similar and satisfactory quality of prediction for both sea states.

These results were obtained using a wave model based on a HOS method. This allows to enjoy the accuracy of fully nonlinear models, while maintaining an efficiency that is still compatible with real-time prediction, in the long run. The method investigated in this work achieved results of comparable quality to previous attempts using HOS methods, with a shorter computation time because only one forward HOS simulation is needed here. In the present work, the computations were conducted with a single processor and no code optimization, and the CPU time was comparable to the simulation time. Considering we were in a model scale tank configuration with a Froude scaling, this means that the prediction is actually obtained faster than real-time at full scale. These are promising results, compared to the existing non-linear approaches.

7. Conclusions

Following on from previous numerical studies (Huchet et al., 2021), this paper reported on the experimental validation of a nonlinear, deterministic wave prediction method, based on wave-induced instantaneous velocity measurements. The method was tested for long-crested, irregular waves with a low steepness, as an experimental proof of concept. The experiments were conducted in a towing tank using wave probes, a single-point ADV velocity sensor and two ADCP velocity profilers, the latter instruments being originally designed to be deployed at sea. A dedicated method combined the velocity sensors measurements to retrieve the instantaneous, horizontal velocity profile, which was not directly accessible using conventional equipment. This profile was used as a forcing field in the nonlinear wave propagation model HOS-NWT $_{pred}$, to generate and propagate the corresponding sea state, and to produce a prediction of the free surface elevation. The prediction obtained was compared with the measurements of the wave probes. We evaluated the overall feasibility of the prediction method in two parts: first, we assessed the quality of the instantaneous horizontal velocity profiles retrievable from the acoustic instruments; then, we examined the quality of the surface elevation prediction obtained using this information on the sea state.

This study was conducted under challenging conditions due to the use of ADCPs in a lab environment with fresh, clear water. Because of this, the quality of the velocity data measured was not consistent across all trials.

Still, this work describes the first experimental proof of concept of a new prediction algorithm, and gave promising results. When good measuring conditions were ensured, the reconstruction step proved able to provide a satisfying horizontal velocity profile, using imperfect velocity data from the upper part of the water column only. From this reconstructed profile, the wave model generated good quality

predictions of free surface elevation. In particular, the phase error on the predicted waves remained very small even several peak wavelengths downstream the measurements location. This allows a longer prediction horizon and is also an important aspect when developing control strategies for wave energy converters or floating offshore wind turbines.

These results are promising for practical applications, as the method allows the use of nonlinear propagation while getting rid of the time-consuming assimilation procedure usually needed to initialize such nonlinear models. This, combined with the efficiency of an HOS propagation model, significantly reduces the CPU time needed to get a prediction, compared to other nonlinear prediction algorithms.

Further work should include the extension of the method to multi-directional wave prediction. Even with several instruments deployed, the data collected will not provide a full knowledge of the multi-directional sea state and some assumptions on its characteristics will be needed. There is also room for improvement in using more effectively the information already available from the measuring devices: in the present study, only the central beam of the ADCPs was used. The slanted beams could be a valuable complementary source of information as well, provided a suitable processing method is developed to handle and combine the different sources of information.

CRedit authorship contribution statement

Marion Huchet: Conceptualization, methodology, software, validation, formal analysis, investigation, data curation, writing – original draft, writing – review and editing, visualization. **Aurélien Barbarit:** Conceptualization, methodology, validation, writing – review and editing, supervision, project administration, funding acquisition. **Guillaume Ducrozet:** Conceptualization, methodology, software, validation, data curation, writing – review and editing, supervision. **Pierre Ferrant:** Conceptualization, methodology, validation, writing – review and editing, supervision. **Jean-Christophe Gilloteaux:** Conceptualization, methodology, validation, writing – review and editing, supervision. **Eloi Droniou:** Validation, writing – review and editing, supervision, funding acquisition.

Declaration of competing interest

The authors declare that they have no known competing financial interests of personal relationships that could have appeared to influence the work reported in this paper.

Acknowledgments

This work was supported by the French *Agence de la transition écologique* (ADEME) and by DynamOcean.

A. ADCP data quality control

A.1. Correlation test

The first processing step rules out data points associated to a bad correlation value. Correlation is a quantity provided directly by the ADCPs for each velocity measurement (i.e., for each cell and each ping) and is a proxy for signal quality. Here, after a close examination of the data set, the minimum acceptable correlation is set to 80%: all velocities with a correlation below this threshold are discarded.

This step leaves very few valid data points in the lower part of the water column. Therefore, velocity measurements are kept only for cells above a custom depth limit. This limit is defined for each trial as the depth below which more than 50% of the data do not pass the correlation test. It generally falls between $z_{lim} = -1.2$ m and -0.8 m.

While allowing to identify many erroneous values, the correlation check still leaves out numerous outliers. The most obvious ones are then detected iteratively and independently for each depth cell, with the following criterion: $W(z, t)$ is an outlier if $|W(z, t) - \langle W(z) \rangle| > 6\sigma_W(z)$, where $\langle W(z) \rangle$ is the mean value taken by $W(z)$ in the considered sample (updated at each iteration).

A.2. Phase-Space Thresholding Method

The resulting velocity data is a partially masked array with missing data in place of outliers. However, in the following steps a complete time array is needed at each cell, so the missing data are filled using 2D cubic interpolation. An iterative Phase-Space Thresholding Method (Goring and Nikora, 2002; Mori et al., 2007) then detects the remaining outliers, and replaces them using cubic interpolation. This step is conducted independently for each depth cell and requires knowledge of the full time series at each cell.

A.3. Vertical fitting

Finally, after outliers have been identified and replaced, a vertical fitting is applied on the resulting W arrays, using a 3-component approximation of the linear expression for W in the Airy wave theory:

$$f(z, a_1, k_1, a_2, k_2, a_3, k_3) = \sum_{i=1}^3 a_i \frac{\sinh[k_i(z+h)]}{\sinh[k_i h]} \quad (9)$$

At each time step, the parameters $(a_1, k_1, a_2, k_2, a_3, k_3)$ are determined using a non-linear least squares method, to find the function that best fits the post-processed experimental W profile between z_{lim} and z_{max} .

After this last step, the measurements of both ADCPs present themselves in the form of checked and processed W fields, over a depth range restricted to $[z_{lim}; z_{max}]$.

References

Adcock, T.A.A., Gibbs, R.H., Taylor, P.H., 2012. The nonlinear evolution and approximate scaling of directionally spread wave groups on deep water. *Proceedings of the Royal Society A: Mathematical, Physical and Engineering Sciences* 468, 2704–2721. URL: <https://royalsocietypublishing.org/doi/full/10.1098/rspa.2012.0029>, doi:10.1098/rspa.2012.0029. publisher: Royal Society.

- Aragh, S., Nwogu, O., 2008. Variation Assimilating of Synthetic Radar Data into a Pseudo-spectral Wave Model. *Journal of Coastal Research* 2008, 235–244. URL: [https://bioone.org/journals/journal-of-coastal-research/volume-2008/issue-10052/1551-5036-52.sp1.235/](https://bioone.org/journals/journal-of-coastal-research/volume-2008/issue-10052/1551-5036-52.sp1.235/Variation-Assimilating-of-Synthetic-Radar-Data-into-a-Pseudo-spectral/) publisher: Coastal Education and Research Foundation.
- Blondel, E., Bonnefoy, F., Ferrant, P., 2010. Deterministic non-linear wave prediction using probe data. *Ocean Engineering* 37, 913–926. URL: <https://www.sciencedirect.com/science/article/pii/S0029801810000661>, doi:10.1016/j.oceaneng.2010.03.002.
- Blondel-Coupré, E., Naaijen, P., 2013. Reconstruction and Prediction of Short-Crested Seas Based on the Application of a 3D-FFT on Synthetic Waves: Part 2 — Prediction, American Society of Mechanical Engineers Digital Collection. pp. 55–70. URL: <https://computationalnonlinear.asmedigitalcollection.asme.org/OMAE/proceedings/OMAE2012/44922/55/268257>, doi:10.1115/OMAE2012-83096.
- Bonnefoy, F., 2005. Modélisation expérimentale et numérique des états de mer complexes. Ph.D. thesis. Ecole Centrale de Nantes (ECN). Nantes, France.
- Bonnefoy, F., Ducrozet, G., Le Touzé, D., Ferrant, P., 2010. Time domain simulation of nonlinear water waves using spectral methods, in: *Advances in Numerical Simulation of Nonlinear Water Waves*. World Scientific. volume 11 of *Advances in Coastal and Ocean Engineering*, pp. 129–164. URL: https://www.worldscientific.com/doi/abs/10.1142/9789812836502_0004, doi:10.1142/9789812836502_0004.
- Desmars, N., Bonnefoy, F., Grilli, S.T., Ducrozet, G., Perignon, Y., Guérin, C.A., Ferrant, P., 2020. Experimental and numerical assessment of deterministic nonlinear ocean waves prediction algorithms using non-uniformly sampled wave gauges. *Ocean Engineering* 212, 107659. URL: <http://www.sciencedirect.com/science/article/pii/S0029801820306557>, doi:10.1016/j.oceaneng.2020.107659.
- Duan, W., Ma, X., Huang, L., Liu, Y., Duan, S., 2020. Phase-resolved wave prediction model for long-crest waves based on machine learning. *Computer Methods in Applied Mechanics and Engineering*, 14.
- Ducrozet, G., 2007. Modélisation des processus non-linéaires de génération et de propagation d'états de mer par une approche spectrale. Ph.D. thesis. Ecole Centrale de Nantes (ECN). Nantes, France.
- Ducrozet, G., Bonnefoy, F., Le Touzé, D., Ferrant, P., 2006. Implementation And Validation of Nonlinear Wavemaker Models In a HOS Numerical Wave Tank. *International Journal of Offshore and Polar Engineering* 16. URL: <https://www.onepetro.org/journal-paper/ISOPE-06-16-3-161>. number: 03.
- Ducrozet, G., Bonnefoy, F., Le Touzé, D., Ferrant, P., 2012. A modified High-Order Spectral method for wavemaker modeling in a numerical wave tank. *European Journal of Mechanics - B/Fluids* 34, 19–34. URL: <http://www.sciencedirect.com/science/article/pii/S0997754612000180>, doi:10.1016/j.euromechflu.2012.01.017.
- Fucile, F., Bulian, G., Lugni, C., 2018. A probabilistic approach for the quantification of prediction error in deterministic phase-resolved wave forecasting. *Ocean Engineering* 163, 718–736. URL: <http://www.sciencedirect.com/science/article/pii/S0029801818305900>, doi:10.1016/j.oceaneng.2018.04.079.
- Furgerot, L., Sentchev, A., Bailly du Bois, P., Lopez, G., Morillon, M., Poizot, E., Méar, Y., Bennis, A.C., 2020. One year of measurements in Alderney Race: preliminary results from database analysis. *Philosophical Transactions of the Royal Society A: Mathematical, Physical and Engineering Sciences* 378, 20190625. URL: <https://royalsocietypublishing.org/doi/full/10.1098/rsta.2019.0625>, doi:10.1098/rsta.2019.0625. publisher: Royal Society.
- Goring, D.G., Nikora, V.I., 2002. Despiking Acoustic Doppler Velocimeter Data. *Journal of Hydraulic Engineering* 128, 117–126. URL: [http://ascelibrary.org/doi/10.1061/\(ASCE\)0733-9429\(2002\)128:1\(117\)](http://ascelibrary.org/doi/10.1061/(ASCE)0733-9429(2002)128:1(117)), doi:10.1061/(ASCE)0733-9429(2002)128:1(117).

- Guerrero, M., 2012. Laboratory validation of acoustic Doppler current profiler (ADCP) techniques for suspended sediment investigations. *Flow Measurement and Instrumentation* , 9.
- Hilmer, T., Thornhill, E., 2015. Observations of predictive skill for real-time Deterministic Sea Waves from the WaMoS II, in: *OCEANS 2015 - MTS/IEEE Washington*, pp. 1–7. doi:10.23919/OCEANS.2015.7404496.
- Huchet, M., Babarit, A., Ducrozet, G., Gilloteaux, J.C., Ferrant, P., 2021. Nonlinear deterministic sea wave prediction using instantaneous velocity profiles. *Ocean Engineering* 220, 108492. URL: <http://www.sciencedirect.com/science/article/pii/S0029801820313998>, doi:10.1016/j.oceaneng.2020.108492.
- Klein, M., Dudek, M., Clauss, G.F., Hoffmann, N., Behrendt, J., Ehlers, S., 2019. Systematic Experimental Validation of High-Order Spectral Method for Deterministic Wave Prediction, American Society of Mechanical Engineers Digital Collection. URL: <https://energyresources.asmedigitalcollection.asme.org/OMAE/proceedings/OMAE2019/58851/V07BT06A056/1067933>, doi:10.1115/OMAE2019-95063.
- Kusters, J., Cockrell, K., Connell, B., Rudzinsky, J., Vinciullo, V., 2016. FutureWaves™: A real-time Ship Motion Forecasting system employing advanced wave-sensing radar, in: *OCEANS 2016 MTS/IEEE Monterey*, pp. 1–9. doi:10.1109/OCEANS.2016.7761478.
- Köllisch, N., Behrendt, J., Klein, M., Hoffmann, N., 2018. Nonlinear real time prediction of ocean surface waves. *Ocean Engineering* 157, 387–400. URL: <https://www.sciencedirect.com/science/article/pii/S0029801818303184>, doi:10.1016/j.oceaneng.2018.03.048.
- Le Touzé, D., 2003. Méthodes spectrales pour la modélisation non-linéaire d'écoulements à surface libre instationnaires. Ph.D. thesis. Ecole Centrale de Nantes (ECN). Nantes, France.
- Mansard, E.P.D., Funke, E.R., 1980. The Measurement of Incident and Reflected Spectra Using a Least Squares Method , 154–172URL: <https://ascelibrary.org/doi/10.1061/9780872622647.008>, doi:10.1061/9780872622647.008. publisher: American Society of Civil Engineers.
- Molin, B., 2002. Hydrodynamique des structures offshore. Editions TECHNIP. Google-Books-ID: ynsq9BLf0kEC.
- Mori, N., Suzuki, T., Kakuno, S., 2007. Noise of Acoustic Doppler Velocimeter Data in Bubbly Flows. *Journal of Engineering Mechanics* 133, 122–125. URL: [https://ascelibrary.org/doi/full/10.1061/\(ASCE\)0733-9399\(2007\)133:1\(122\)](https://ascelibrary.org/doi/full/10.1061/(ASCE)0733-9399(2007)133:1(122)), doi:10.1061/(ASCE)0733-9399(2007)133:1(122). publisher: American Society of Civil Engineers.
- Muste, M., Kim, D., González-Castro, J.A., 2010. Near-Transducer Errors in ADCP Measurements: Experimental Findings. *Journal of Hydraulic Engineering* 136, 275–289. URL: [http://ascelibrary.org/doi/10.1061/\(ASCE\)1084-0699\(2010\)136:3\(275\)](http://ascelibrary.org/doi/10.1061/(ASCE)1084-0699(2010)136:3(275)), doi:10.1061/(ASCE)1084-0699(2010)136:3(275).
- Naaijen, P., van Oosten, K., Roozen, K., van 't Veer, R., 2018. Validation of a Deterministic Wave and Ship Motion Prediction System, American Society of Mechanical Engineers Digital Collection. URL: <https://asmedigitalcollection.asme.org/OMAE/proceedings/OMAE2018/51272/V07BT06A032/274143>, doi:10.1115/OMAE2018-78037.
- Naaijen, P., Trulsen, K., Blondel-Coupré, E., 2014. Limits to the extent of the spatio-temporal domain for deterministic wave prediction. *International Shipbuilding Progress* 61, 203–223. URL: <http://content.iospress.com/articles/international-shipbuilding-progress/isp113>, doi:10.3233/ISP-140113. number: 3-4.
- Naaijen, P., Wijaya, A.P., 2014. Phase Resolved Wave Prediction From Synthetic Radar Images, American Society of Mechanical Engineers Digital Collection. URL: <https://asmedigitalcollection.asme.org/OMAE/proceedings/OMAE2014/45509/V08AT06A045/279048>, doi:10.1115/OMAE2014-23470.
- Nortek, 2022a. Comprehensive Manual for Velocimeters.
- Nortek, 2022b. Signature Principles of Operation. URL: <https://support.nortekgroup.com/hc/en-us/articles/360029835831-Principles-of-Operation-Signature>.
- Qi, Y., Wu, G., Liu, Y., Yue, D.K.P., 2018. Predictable zone for phase-resolved reconstruction and forecast of irregular waves. *Wave Motion* 77, 195–213. URL: <http://www.sciencedirect.com/science/article/pii/S0165212517301518>, doi:10.1016/j.wavemoti.2017.12.001.
- Rusello, P.J., 2009. A Practical Primer for Pulse Coherent Instruments. Technical Report TN-07. Nortek AS.
- Simanesev, A., Trulsen, K., Krogstad, H.E., Nieto Borge, J.C., 2017. Surface wave predictions in weakly nonlinear directional seas. *Applied Ocean Research* 65, 79–89. URL: <https://www.sciencedirect.com/science/article/pii/S0141118716303613>, doi:10.1016/j.apor.2017.03.009.
- Toffoli, A., Onorato, M., Bitner-Gregersen, E., Osborne, A.R., Babanin, A.V., 2008. Surface gravity waves from direct numerical simulations of the Euler equations: A comparison with second-order theory. *Ocean Engineering* 35, 367–379. URL: <https://www.sciencedirect.com/science/article/pii/S0029801807002168>, doi:10.1016/j.oceaneng.2007.10.004.
- Trulsen, K., Stansberg, C.T., 2001. Spatial Evolution of Water Surface Waves: Numerical Simulation And Experiment of Bichromatic Waves, OnePetro. URL: <https://onepetro.org/ISOPEIOPEC/proceedings/ISOPE01/All-ISOPE01/ISOPE-I-01-247/7968>.
- West, B.J., Brueckner, K.A., Janda, R.S., Milder, D.M., Milton, R.L., 1987. A new numerical method for surface hydrodynamics. *Journal of Geophysical Research: Oceans* 92, 11803–11824. URL: <https://agupubs.onlinelibrary.wiley.com/doi/abs/10.1029/JC092iC11p11803>, doi:10.1029/JC092iC11p11803. number: C11.
- Wu, G., 2004. Direct simulation and deterministic prediction of large-scale nonlinear ocean wave-field. Thesis. Massachusetts Institute of Technology. URL: <http://dspace.mit.edu/handle/1721.1/33450>.
- Yoon, S., Kim, J., Choi, W., 2016. An Explicit Data Assimilation Scheme for a Nonlinear Wave Prediction Model Based on a Pseudo-Spectral Method. *IEEE Journal of Oceanic Engineering* 41, 112–122. doi:10.1109/JOE.2015.2406471. conference Name: IEEE Journal of Oceanic Engineering.
- Zakharov, V.E., 1968. Stability of periodic waves of finite amplitude on the surface of a deep fluid. *Journal of Applied Mechanics and Technical Physics* 9, 190–194. URL: <https://doi.org/10.1007/BF00913182>, doi:10.1007/BF00913182. number: 2.
- Zhang, H.D., Ducrozet, G., Klein, M., Guedes Soares, C., 2017. An experimental and numerical study on breather solutions for surface waves in the intermediate water depth. *Ocean Engineering* 133, 262–270. URL: <https://www.sciencedirect.com/science/article/pii/S0029801817300458>, doi:10.1016/j.oceaneng.2017.01.030.
- Zhang, J., Zhao, X., Jin, S., Greaves, D., 2022. Phase-resolved real-time ocean wave prediction with quantified uncertainty based on variational Bayesian machine learning. *Applied Energy* 324, 119711. URL: <https://linkinghub.elsevier.com/retrieve/pii/S0306261922010042>, doi:10.1016/j.apenergy.2022.119711.